Tungsten Trioxide Nanowires Decorated with Iridium Oxide Nanoparticles as Gas Sensing Material

Eric Navarrete[1], Carla Bittencourt[2], Polona Umek[3], Damien Cossement[4] , Frank Güell[5], Eduard Llobet*[1]

[1]MINOS-EMaS, Universitat Rovira i Virgili, Avda. Països Catalans, 26, 43007 Tarragona, Spain

[2]Chimie des Interactions Plasma – Surface (ChIPS), Research Institute for Materials Science and Engineering, Université de Mons, Avenue Copernic 3, 7000 Mons, Belgium

[3]Jožef Stefan Institute, Jamova cesta 39, 10000 Ljubljana, Slovenia.

[4] Materia Nova, Avenue Copernic 3, 7000 Mons, Belgium

[5]ENFOCAT-IN[2]UB, Universitat de Barcelona, C/Martí i Franquès 1, 08028 Barcelona, Catalunya, Spain

*Correspondence: eduard.llobet@urv.cat; Tel.: +34 977 558 502

Abstract

Tungsten trioxide nanowires were grown employing aerosol assisted chemical vapor deposition (AACVD) and subsequently decorated with different loading levels of iridium oxide nanoparticles. AACVD has been already demonstrated to be a useful tool to load different ranges of nanoparticles on top of an already grown layer. This procedure enables growing the gas sensitive nanomaterials directly onto application substrates for the development of chemo-resistive gas sensors. The morphology and composition of the different materials were characterized via different techniques. It was found that iridium oxide loading resulted in remarkable changes in the morphology and defects of tungsten oxide nanowires. The gas sensing properties of such layers were studied towards ethanol or ammonia vapors, hydrogen, hydrogen sulfide, and nitrogen dioxide. The optimization of the operating temperature and the level of iridium oxide loading results in an improvement in the responsiveness and selectivity towards the species tested. In particular, a dramatically high increase in the response towards nitrogen dioxide is achieved. The mechanisms of gas sensing are discussed in detail.

Keywords: Tungsten Oxide, Iridium Oxide, Nanowires, Nanoparticles, Gas Sensing, NO_2.

1. Introduction

There is a worldwide rising concern about air quality monitoring and toxic gas emissions. In this field, extensive efforts have been made in order to discover or manufacture sensors, with the ability to detect a specific gas among a mixture of gases or sensors having the ability to continuously monitor an atmosphere. Semiconductor metal oxides (MOXs) have risen as an outstanding family of promising materials due to their inexpensiveness, outstanding properties, such as chemical resistance, endurance and time stability. MOXs are employed as

sensitive layers for sensors in many fields, they are present mostly in the automotive industry, the petrochemical industry and for safety monitoring in domestic premises. One of the most representative examples are MOX sensors employing SnO_2 nanolayers for the indoor detection of CO [1].

N-type semiconductor metal oxides often used for gas sensing such as SnO_2, ZnO, TiO_2, V_2O_4, In_2O_3 or WO_3, present different morphologies depending on the synthesis technique employed. From the abovementioned (MOXs), WO_3 has been extensively researched during the last decades for its outstanding photocatalytic and sensing properties. WO_3 presents a band gap of 2.6 eV, and can be tailored in different nanostructures depending on the growth methodology. WO_3 presents different crystallinity depending on temperature. For example ε-WO_3 with a monoclinic structure (P_m) is the predominant structure between 0 and 230 K. Between 230 and 290 K δ-WO_3 is the predominant structure belonging to the triclinic system (P_{-1}) and, finally, the predominant structure between 290 and 600 K is monoclinic γ-WO_3 belonging to the P2/m spatial group [2].

There are many approaches to synthesize nanostructured layers of WO_3 with different morphologies. The first family of techniques is the liquid-phase synthesis (LPS). In the liquid-phase approach, thin films are usually obtained, even though the product obtained is mostly a hydrate of tungsten trioxide, which will need further steps of calcination/annealing to become fully oxidized. Another approach consist of using hard templates [3] or soft templates [4], a variation of the sol-gel methodology in which porous thin films of WO_3 can be obtained, yet there is also the need of further annealing steps. Hydrothermal treatment is the most attractive LPS to tailor 1-D WO_3 nanostructures such as nanoplates [5] or nanowires/nanorods [6] through an easy procedure. A second family of procedures can be englobed to vapor-phase synthesis (VPS). In this family there are both chemical and physical approaches such as vapor phase deposition or sputtering. These two aforementioned techniques can produce

different nanostructured WO_3 materials. In VPS, nanoparticles, nanorods, thin or thick films can be produced once the correct temperatures, gas flows and precursors are set [7]. For example, sputtering, glancing angle sputtering or oxygen reactive sputtering enables the fabrication of compact, nanostructured or thin metal oxide films, which can be height controlled [8]. Despite the fact that there are several VPS techniques, chemical vapor deposition (CVD) outstands as an easy procedure to obtain a wide range of WO_3 morphologies when using the appropriate conditions [9].

In this work we employ a modification of the above mentioned CVD, in which the precursors are conveyed dissolved in an aerosol into the reactor in which the CVD process is conducted. In aerosol assisted chemical vapor deposition, an organic solution precursor is prepared and then brought to an aerosol with a high-frequency generator. This aerosol is carried towards a preheated hot-wall reactor where a substrate is placed and the growth will take place. As described by Yun-Tsung et al. the supersaturated vapor containing WO_x condenses on top of the substrate forming WO_x clusters, which will act as seeds to develop the growth of nanowires (NWs) [9]. Thanks to the high temperature present inside the reactor (350 to 400ºC) the organic solvents rapidly decompose and leave WO_x species to act as growing blocks to keep forming the NW structure. Due to the organic precursors used, some remnant amorphous carbon is also present in the NWs forest layer, which is removed in a subsequent annealing step. The AACVD methodology can be employed as well to deliver foreign oxide nanoparticles to sensing layers previously grown. This makes the AACVD a suitable methodology for obtaining pure or late-transition metal oxide loaded tungsten oxide NWs. Typically, extensive research has been done employing noble metals and metal oxides onto tungsten oxide nanowires for gas sensing. For example, Annanouch et al. synthesized, via AACVD, tungsten oxide NWs decorated with core-shell Pd-PdO NPs for the detection of H_2 [10]. Platinum and gold have been

also reported by Vallejos et al. [11] for the detection of H_2. Non-noble metals such as copper have been studied and reported by Annanouch et al. as highly selective materials for the detection of H_2S [12] and, nickel oxide reported by Navarrete et. al. has also been demonstrated to increase the selectivity towards H_2S [13]. Despite the fact that noble metals display excellent gas sensing properties when decorating tungsten oxide NWs, to the authors' knowledge, iridium oxide has been studied very seldom in the context of gas sensing. Karthigeyan and co-workers presented a field effect transistor employing an iridium oxide thin film as ammonia gas sensor at room temperature [14]. However, studying this material is of interest, since iridium oxide has been widely reported as electrode material, due to its high catalytic activity in water-splitting reactions (OER), or as a pH sensor.

2. Experimental

2.1. Materials synthesis

Pure tungsten oxide (WO_3) NWs and IrO_2-decorated WO_3 NWs were grown employing the AACVD. The precursor for WO_3 NWs was tungsten hexacarbonyl ($W(CO)_6$) (97% purity) purchased from Sigma-Aldrich and the Iridium (IV) oxide (IrO_2) powder (purity 99%) was purchased from Alfa Aesar. Both precursors were employed without further purification. To grow such structures, two approaches can be considered: a 1-Step or 2-Step methodology. In the 1-Step methodology, both the NWs precursor and the iridium oxide are mixed in the same solution and delivered to the reactor during a single deposition. This 1-Step methodology has been already studied in previous works [13] and has been demonstrated to have a low-loading capacity in comparison to the 2-Step methodology, which is a much efficient way to achieve higher loading levels of tungsten oxide nanowires. Therefore, the 2-Step methodology was implemented.

In the first step, a solution of $W(CO)_6$ is prepared mixing 50 mg $W(CO)_6$ with 15 ml of acetone and 5 ml methanol. This solution then is converted into a spray

of micro-droplets employing sonication at high frequency. Once the aerosol is created, a flow of nitrogen is used at 0.5 L/min to carry it towards a preheated hot wall CVD reactor. In this particular work, the optimal growth temperature for NWs lies in the range between 370 and 400 ºC, since lower temperatures lead to the formation of nano-clustered WO_3 films instead of NWs. In this bottom-up methodology we take advantage of the self-assembly process that occurs once the organic compounds carried by the droplets enters into the high temperature zone were the carbon-based solvents are burned leaving tungsten species that act as building blocks for the NWs. The NW deposition took place onto the electrode area (2.5 x 2.5 mm^2) of commercially available alumina transducers (Ceram Tech GmBH, Plochingen, Germany).

Once the chemical vapor deposition is finished, the material is let to cool down at room temperature and examined. Due to the use of organic precursors and solvents, the tungsten trioxide NW layers have a dark blue color. This color is attributed to the presence of amorphous carbon and to a non-stoichiometric WO_{3-x}. To remove carbon impurities and increase the oxidation of tungsten, an annealing step is carried out. The annealing takes place inside a muffle with a synthetic air flow at 2 L/min during 2 h at 500 ºC, heated at 5 ºC/min rate and cooled naturally to room temperature once the process is finished. Finally, the annealed NWs show a yellow-pale color attributed to an almost stoichiometric WO_3 and to the removal of most carbon contamination. As mentioned above, such methodology can be employed also to load different amounts of nanoparticles to already grown NW layers. Following the same procedure several organic solutions were prepared depending on the desired iridium oxide concentration. Different amounts of iridium oxide (i.e., 5 mg, 10 mg and 15 mg) were dispersed in 10 ml methanol. The particle suspension solution was transformed in an aerosol and carried towards the preheated reactor where an already coated sensor had been placed. A commercially available iridium oxide

characterized by a very wide dispersion in the dimensions of IrO_2 particles was used. However, the ultrasonic generator produced an aerosol in which only the smaller (nanosized) IrO_2 particles could be found. These were the particles that were dragged by the carrier gas flow into the reactor and became eventually deposited onto WO_3 nanowires (see the supporting information). Bigger (i.e., heavier) particles remained in the vessel in which the aerosol was generated and these could be recycled, after mechanical milling, in a new loading process. Subsequently to the iridium oxide loading step, another annealing step is implemented to remove the remnant carbon impurities.

The morphology, crystalline phase and chemical composition of the different sensors grown on top of each substrate were studied employing scanning electron microscope (SEM) and high resolution transmission electron microscope (HRTEM), X-ray diffraction (XRD), energy-dispersive X-ray spectroscopy (EDX) and X-ray photoelectron spectroscopy (XPS). SEM images were acquired using a SU8020 Microscope from Hitachi and a JEOL 7600F field emission SEM (15 kV, working distance of 15 mm). The image resolution was set to 512 × 384 pixels while the corresponding map resolution was set to 128 × 96 pixels, meaning a pixel size of 0.01 μm in the image and of 0.05 μm in the map. EDX spectra were acquired using a microanalysis tool from Oxford Instruments by scanning a selected area of the sample (pixel resolution as for the SEM analysis) at a working distance of 10 mm at 20 kV with a 137 eV resolution. EDX spectra were analyzed with the aid of the INCA software. HRTEM characterization of the samples was performed on a Jeol 2100 microscope, working at 200 kV. The material was scratched from its alumina substrate and dispersed in methanol. The dispersion was ultrasonicated for 20 minutes and a drop was deposited on a lacy carbon film supported by a nickel grid. XRD was performed employing a Bruker-AXS D8-Discover diffractometer equipped with parallel incident beam (Göbel mirror), vertical θ-θ goniometer, XYZ motorized stage, and a General Area Detector

Diffraction System. A 500 μm X-ray collimator system allowed the analysis of a mean area represented by an ellipsoid with a constant short axis of 500 μm and a variable long axis of 1500 down to 600 μm. The X-ray diffractometer was operated at 40 kV and 40 mA to generate Cu Kα radiation. The detector was an HI-STAR (multiwire proportional counter of 30 cm × 30 cm with a 1024 × 1024 pixel grid) placed at a 15-cm distance from the sample. Experimental diffractograms were fitted with the crystal structure (Rietveld analysis) for the phases identified with the aid of TOPAS 5.0 software. XPS was conducted using a VERSAPROBE PHI 5000 from Physical Electronics, equipped with a monochromatic Al Kα X-ray source (1486.6 eV). The X-ray photoelectron spectra were collected at the take-off angle of 45° with respect to the electron energy analyzer operated in the CAE (constant analyzer energy) mode, the X-ray beam diameter was 200 μm and the pass energy used was 187.5 eV for recording the survey spectrum and 23.5 eV for core level analysis. For the compensation of built-up charge on the sample surface during the measurements, a dual beam charge neutralization composed of an electron gun (≈1 eV) and an Ar ion gun (≤10 eV) was used. Binding energies are all referred to the C1s peak at 284.6 eV. Static ToF-SIMS data were acquired in negative mode using a ToF-SIMS IV instrument from ION-TOF GmbH. An Ar^+ 10 keV ion-beam was used as analysis beam at a current of 0.7 pA (negative ion mode detection), and rastered over a scan area of 100 × 100 μm^2. Three different locations on the surface were accounted for ToF-SIMS analysis.

Room-temperature photoluminescence (PL) measurements were made with a chopped Kimmon IK Series He-Cd laser (325 nm). Fluorescence was dispersed with a Princeton Instruments Acton SP2750 0.750 m imaging triple grating monochromator, detected using a Hamamatsu H8259-02 with a socket assembly E717-500 photomultiplier, and amplified through a Stanford Research Systems SR830 DSP. A 360 nm filter was used to filtering the stray light. It is worth

pointing out that the emission spectra were corrected using the optical transfer function of the PL setup.

2.2. Gas sensing study

To study the tungsten trioxide NW ability to detect gases, and the effect of loading iridium oxide onto the NW matrix, the sensors were exposed to 5 different gases; ammonia vapors, ethanol, hydrogen, hydrogen sulfide and nitrogen dioxide. To perform the gas sensing analysis the sensors were placed inside an airtight Teflon® chamber. In this study all gases employed were used from calibrated gas bottles balanced in dry air and the carrier gas was zero-grade dry air. Despite using dry gases, there is always some remnant humidity in the measurement ring. By using a commercially available humidity sensor (SHT71, from Sensirion AG, Switzerland) placed in the sensor chamber, it was established that the relative humidity ranged between 2% and 5%. The concentrations analyzed for ammonia, ethanol vapors, hydrogen and hydrogen sulfide were set to 5, 10, 15 and 20 ppm and for nitrogen dioxide were set to 250, 500, 750 and 1000 ppb. The concentrations were delivered to the gas chamber through a computer-controlled mass-flow system to ensure the reproducibility of the concentrations delivered. The gas analysis was set as pulses consisting of increasing target gas concentrations with intercalated steps of dry air to recover the baseline at a 100 mL min^{-1} constant flow. The sensor DC electrical resistance was measured, acquired and stored employing a Keysight 3972A data acquisition system. An Agilent U8001A was used as power supply for heating the resistors in order to achieve the operating temperatures of 150 ºC, 200 ºC or 250 ºC. Finally, to analyze the interference of ambient humidity, a liquid mass-flow was employed to humidify the carrier gas (to 35% R.H.) and an Arduino controlling the SHT71 humidity and temperature sensor IC was employed to acquire and store the relative humidity data.

3. Results and discussion

3.1. Effective loading study

Previous research done in the group revealed that different loading concentrations can enhance or decrease the response obtained from different gases [13], as well it has been also reported in the bibliography that higher foreign NPs loadings result in a signal decrease [15]. Therefore, in order to determine if it was worth studying all three loading concentrations in depth an initial screening of gas sensing properties was conducted. In this first step, the concentration tested were pristine WO_3 NWs, and 5, 10 and 15 mg IrO_2 loaded NWs. The overall results showed that for all the gases tested 15 mg IrO_2 loaded NWs had a resistance of the order of 30 GigaOhms. Such high a resistance makes very difficult to measure the sensor response towards a gas. As mentioned above, different loading levels can enhance or decrease the sensor response signal towards a gas. According to these preliminary results, the range of IrO_2 loadings achieved is enough to explore/optimize the gas sensing behavior of the loaded nanomaterials. Figure 1 shows the normalized resistance responses to NO_2 and ethanol as examples of the sensor behavior to oxidizing and reducing gases.

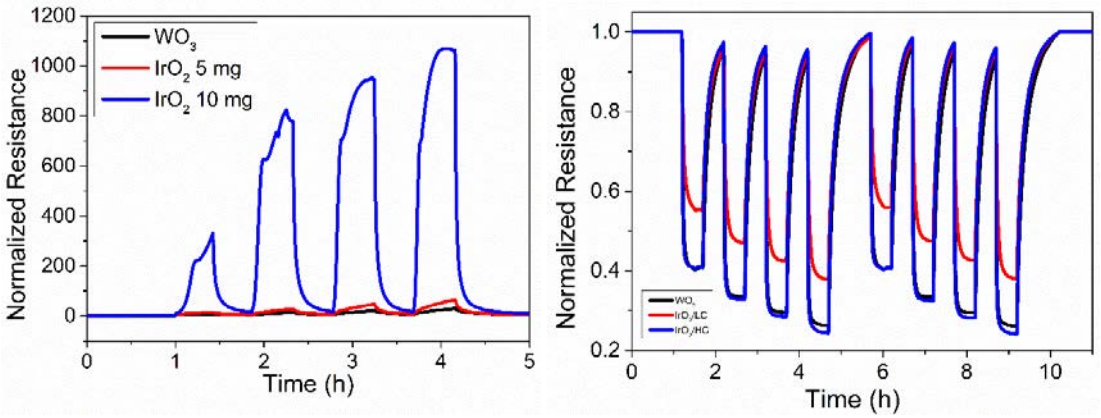

Figure 1. Normalized dynamic response and recovery cycles of sensors. The left panel corresponds to NO_2 measurements obtained at 150 ºC. The right panel corresponds to ethanol measurements obtained at 250 ºC.

Taking into consideration the high resistance of samples loaded with 15 mg IrO_2, only the samples consisting of pure WO_3 NWs, IrO_2 5mg loaded WO_3 NWs and IrO_2 10 mg loaded WO_3 NWs will be further analyzed in depth both

morphologically and chemically. These samples will be referred to, from here on, as WO_3, IrO_2/LC and IrO_2/HC, respectively.

3.2. Nanomaterial characterization

The NWs were analyzed by XRD to obtain the crystallographic structure of pure and IrO_2-loaded WO_3 NWs. The diffraction pattern of the pure WO_3 NW sample shown in figure 2 corresponds to a monoclinic structure, space group $P21/n$ fitting with the ICDD card nº 43-1035. Peaks from the alumina substrate are also present in XRD spectra.

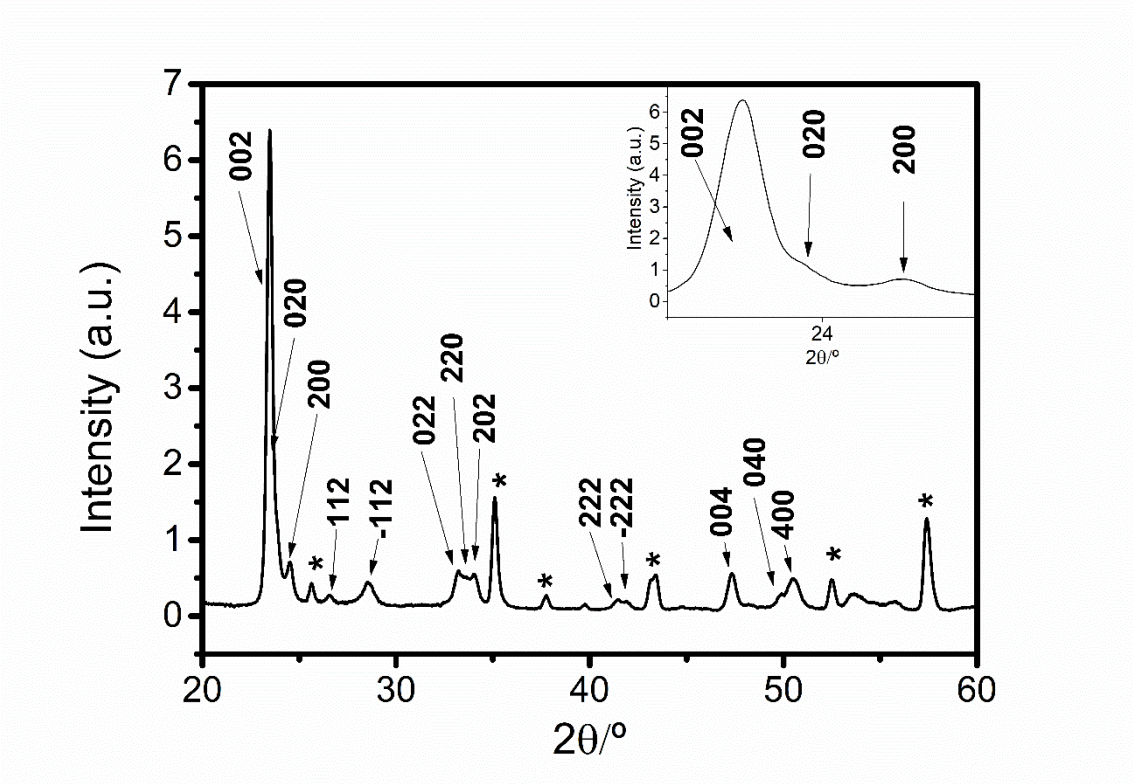

Figure 2. XRD spectrum recorded on a layer of pristine tungsten trioxide NWs on top of an alumina substrate. All data fitted well with the ICDD card 43-1035 and the (*) labelled peaks correspond to the alumina substrate. The inset corresponds to an enlargement of the first two peaks.

Tungsten trioxide NWs loaded with iridium oxide were studied employing SEM to understand their morphology. Figure 3 shows both low and high concentration loaded NWs and their differences. On the one hand, pure WO_3 NWs show a smooth surface with few to none attached material particles (see supporting information Figure S4), on the other hand, IrO_2/LC NWs present

nanoclusters homogenously spread along the body, meanwhile IrO_2/HC NWs show an increase of such nanoclusters with a higher spread along the NW body.

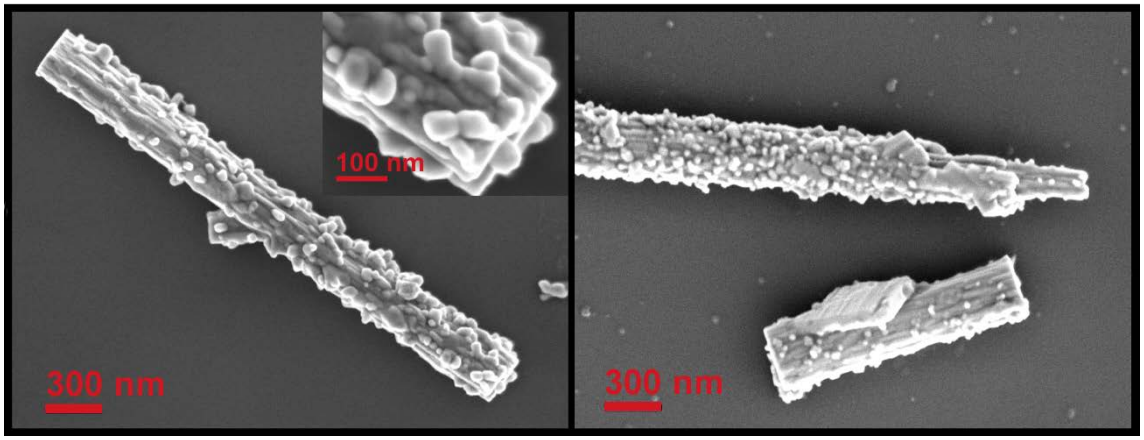

Fig 3. SEM images for; IrO_2/LC NW (left panel), IrO_2/HC NW (right panel).

Then, a HRTEM study was performed in such nanoclusters to determine their morphology, crystallinity and composition. Figure 4, shows an IrO_2/HC NW with a close look to one of such clusters. The HRTEM inset shows that the nanocluster attached to the NW surface is crystalline. The d-spacing between lattice fringes in the inset is 0.364 nm corresponding to (200) planes in WO_3 with monoclinic structure (ICDD 43-1035) confirming the composition of the clusters present in the surface as tungsten trioxide. Therefore, the increase in iridium oxide loading results in a reshape of the NW morphology with the appearance of granular tungsten oxide on the surface of the NWs. This can possibly affect the specific surface area of the nanomaterial and the amount of structural defects.

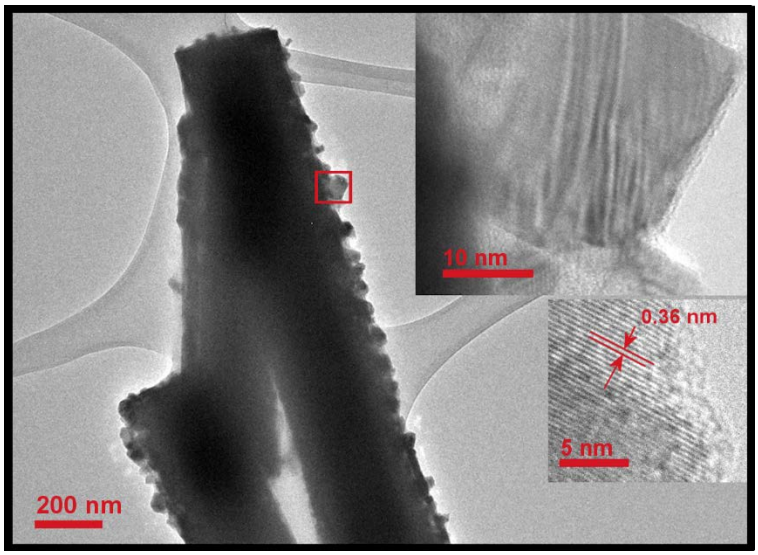

Fig 4. HRTEM image performed on an IrO_2/HC NW (left panel). Close look at the nanoparticle surface showing structured fringes revealing a high crystallinity (Right panel).

X-ray photoelectron spectroscopy and time of flight secondary mass spectrometry were used in the chemical characterization of the sensor active layer. In the XPS survey spectrum we observed tungsten and oxygen peaks, the C 1s peak indicates the presence of contamination that can be associated with the partial removal of organic compounds (see supporting information Figure S5). The most intense Ir XPS peaks partially overlap with the W XPS peaks, as the relative concentration of Ir is expected to be very small (~ 1%), the Ir peaks remain buried under the background of secondary electrons. The presence of Ir at the sample surface was confirmed by ToF-SIMS. We observed the presence of peaks at m/z 238.95 and 240.95 with relative intensity corresponding to the relative isotope abundance of 191 Ir and 193 Ir (Figure 5).

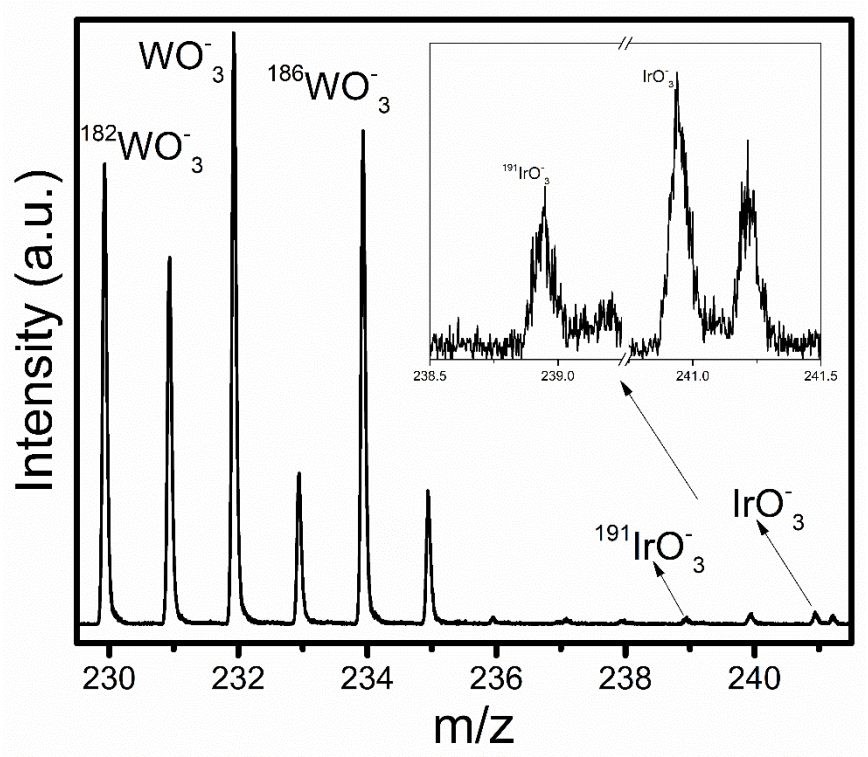

Figure 5. TOF-SIMS surface analysis revealing the presence of iridium oxide at the surface of tungsten trioxide nanowires.

The room-temperature PL spectra are presented in Figure 6. By pumping at 325 nm, we observed an emission peak of the WO_3 NWs at around 450 nm (2.75 eV) with a full width at half maximum (FWHM) of 370 meV. When loading the WO_3 NWs with iridium oxide, the FWHM increased to about 1040 meV. The intensity of each spectrum was normalized to the maximum emission intensity for easiness of comparison. This broadening observed on the FWHM indicates that the quantity of intrinsic defects (e.g. oxygen vacancies and tungsten interstitials) [16]

[17] is higher when loading the WO_3 NWs with iridium oxide nanoparticles, which agrees with the dramatic change in morphology revealed by HRTEM results, see Figure 4, and is a consequence of the larger surface area of the IrO_2-loaded WO_3 NWs respect to the WO_3 NWs [18]. The photoluminescence of iridium oxide was studied to further verify these assumptions. Pure IrO_2 films did not show PL response, which supports the differences observed being due to differences in morphology and defects.

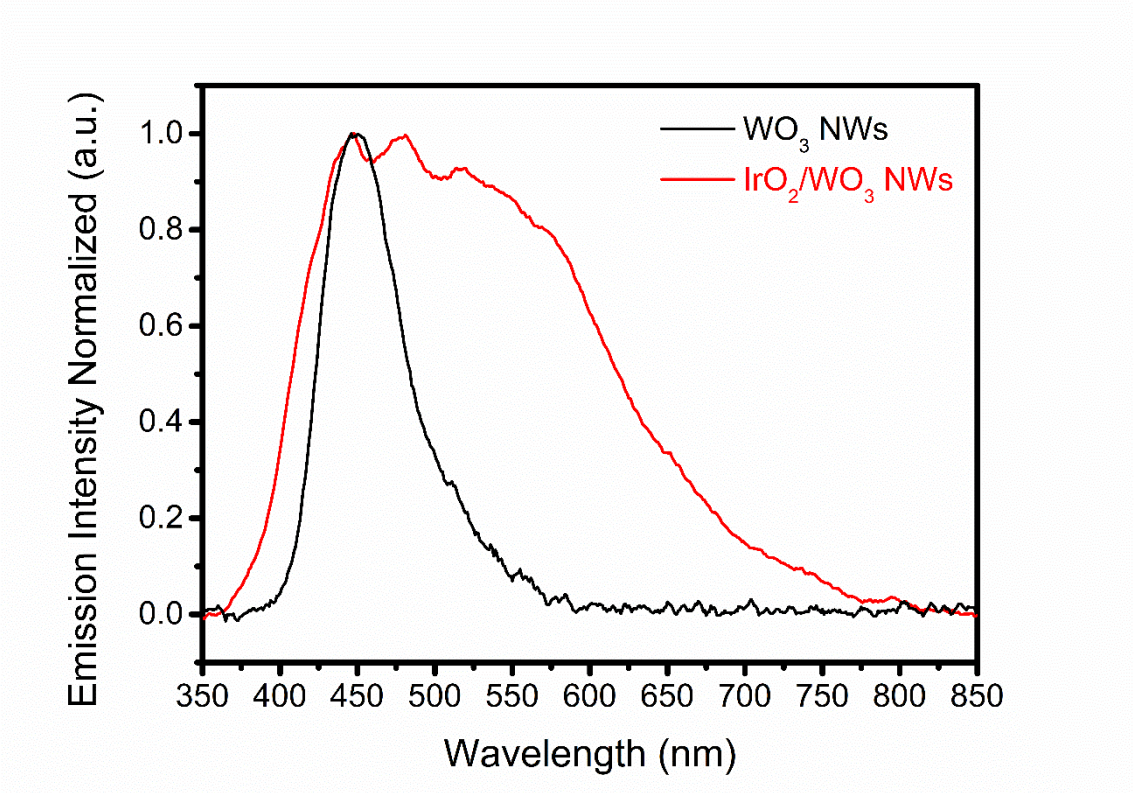

Figure 6. Room-temperature emission spectra for WO_3 NWs and IrO_2-loaded WO_3 NWs.

3.3. Gas sensing responses

The responses towards ethanol, hydrogen sulfide and nitrogen dioxide are presented and discussed in the following paragraphs. The results for hydrogen and ammonia can be found in the supporting information. A table summarizing response times for the different materials and species tested can be found in the supporting information too.

3.3.1. Ethanol results

Sensors were exposed to ethanol vapors balanced in dry air. The results obtained are shown in Figure 7. When operating the sensor at the lower temperature considered (i.e., 150 ºC), the overall responses displayed by all three types of sensors were much lower than the ones recorded at higher temperatures (i.e., 200 ºC or 250 ºC). At 200 ºC or 250 ºC, the response pattern for all the three sensor types shows a similar trend. At the operating temperatures tested, the higher iridium oxide loading level (i.e., IrO_2/HC) slightly enhances ethanol response in comparison to the one obtained with pristine WO_3 NWs, meanwhile the lower iridium oxide loading level (i.e., IrO_2/LC), decreases ethanol response. This behavior can be attributed to a competitive reaction between water vapor and ethanol for the active sites available. At higher loadings of iridium oxide, there is a higher amount of active sites available (due to morphological changes and increased number of defects, as revealed by TEM and PL studies), which enhances the reaction with ethanol molecules.

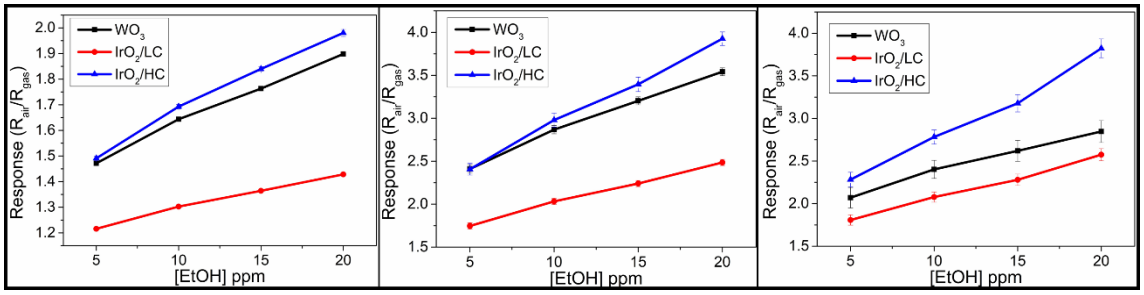

Figure 7. Ethanol detection results at different operating temperatures. From left to right: 150 ºC, 200 ºC and 250 ºC.

3.3.2. Hydrogen sulfide results

Hydrogen sulfide was studied at concentrations ranging from 5 to 20 ppm. The concentrations studied have been decreased in comparison to previous studies performed in our group due to the negative impact that H_2S may have to sensing layers [13]. As it can be seen from Figure 8, the overall responses for all three gas sensor types increase as the operating temperatures are increased. From the results obtained it can be concluded that loading iridium oxide to the nanowire

matrix has little effect on the responses towards hydrogen sulfide. The sensitivity achieved for this type of loading material is significantly lower than the one obtained in previous studies employing copper oxide [12] or nickel oxide [13].

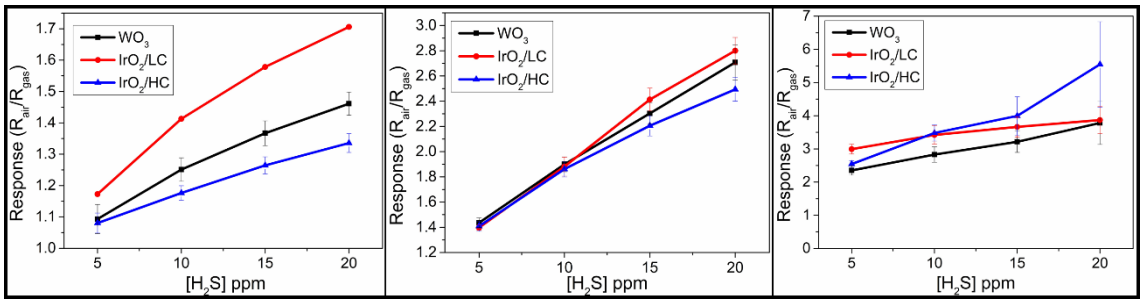

Figure 8. Hydrogen sulfide detection responses at different working temperatures. From left to right panels: 150 ºC, 200 ºC and 250 ºC.

3.3.3. Nitrogen dioxide results

In view of analyzing the response of iridium oxide loaded tungsten oxide NWs towards oxidizing gases, the response to NO_2 was studied. Figure 9 summarizes the results obtained with the three different sensor types studied. The loading with iridium oxide clearly enhances the response towards NO_2. At the lowest temperature tested (i.e., 150 ºC) the response to 1 ppm of NO_2 increases by a factor of 2 for IrO_2/LC and by a factor of 14 for IrO_2/HC (taking as reference the response of pristine tungsten oxide NWs). At the operating temperature of 200 ºC, the highest response for both IrO_2/LC and IrO_2/HC sensor types is achieved (registering 2.3-fold and 95-fold increases in NO_2 response for IrO_2/LC and IrO_2/HC samples, respectively).

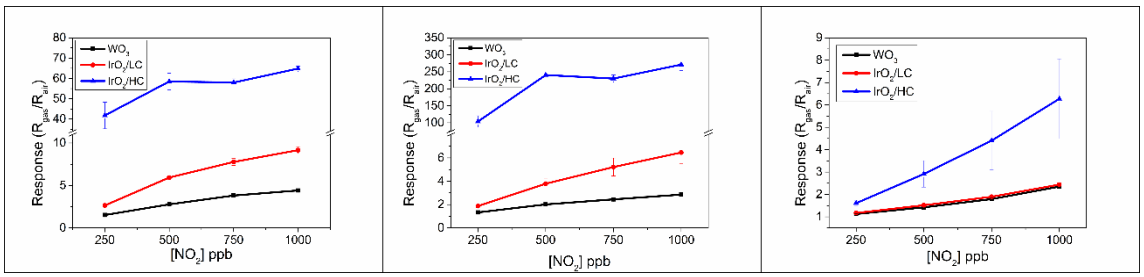

Figure 9. Nitrogen dioxide responses under dry air conditions at different working temperatures. From left to right panels: 150 ºC, 200 ºC and 250 ºC.

3.3.3.1. Humidity effect on the response towards nitrogen dioxide

So far, the analysis of the gas sensing properties has been conducted under dry air conditions. This implies that the actual relative humidity (R.H.) level in the gas-flow measurement set up ranges from 2% up to 5%. However, to emulate real environmental working conditions, measurements conducted at higher R.H. levels are necessary. To do so, different concentrations of NO_2 diluted in dry air were humidified at 35% R.H. and measured. The results are summarized in Figure 10. They reveal that the presence of moisture results in a decrease in the response towards NO_2. This applies for all three type of sensors studied (i.e., pristine WO_3, IrO_2/LC and IrO_2/HC). Despite these results, IrO_2/LC samples displayed the highest and most stable responses towards NO_2 (higher sensitivity) at the three working temperatures studied.

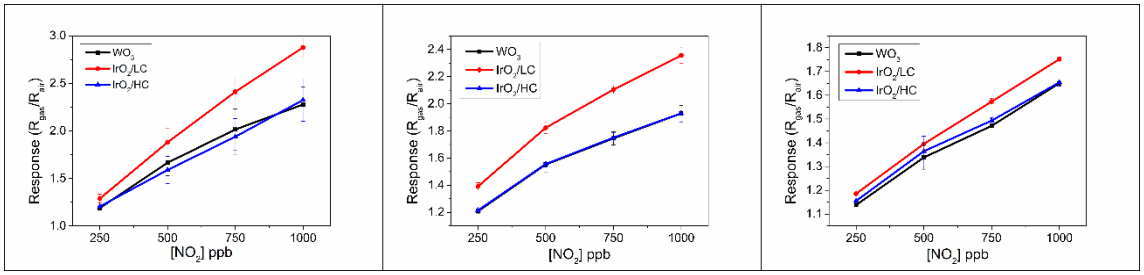

Figure 10. Nitrogen dioxide responses under 35% R.H. conditions at different working temperatures. From left to right: 150 ºC, 200 ºC and 250 ºC.

3.4. Detection mechanisms for nitrogen dioxide

Iridium oxide has been reported as an outstanding material to act as electrode for the oxygen evolution reaction (OER) in water splitting. This reaction occurs at over potentials that range from 1.3 V to 1.6 V, however, the use of metal oxide catalysts can decrease these values, as has been demonstrated in the literature [19]. Iridium oxide belongs to the rutile-type oxides such as RuO_2, MnO_2, PtO_2 [20]. Due to their morphology, non-stoichiometry, band structure and surface electronic structure, these metal oxides display attractive characteristics to be used as materials for electrodes. Considering water splitting on iridium oxide modified electrodes, the OER involves the adsorption of water molecules onto iridium oxide nanoparticles and their reaction with hydroxyls present on the

surface of the metal oxide, giving rise to -OOH transition species [21]. During the OER the oxidation states of iridium playing a role are (III), (IV) and (V). The stable oxidation states (i.e., at the end of the OER) present on the surface are Ir (III) and (IV). Iridium (V) has been reported to be a transition oxidation state found only while the OER is occurring [20].

Therefore, Figure 11 represents the typical mechanism explaining the behavior of iridium oxide during the water splitting oxidation of one water molecule. In this mechanism, water and radical hydroxyl groups adsorb in the first place on the surface of iridium oxide (**S1**) and, subsequently, when another water molecule interacts with the hydroxyl layer, the OER takes place generating a molecular oxygen species (**S2**). This mechanism is supported by experimental data via baseline resistance measurements performed under very low humidity (i.e. <3% R.H.) and humid (35% R.H.) conditions for pure and IrO_2 loaded tungsten oxide sensors (see Fig. S8 and associated discussion in the supporting information).

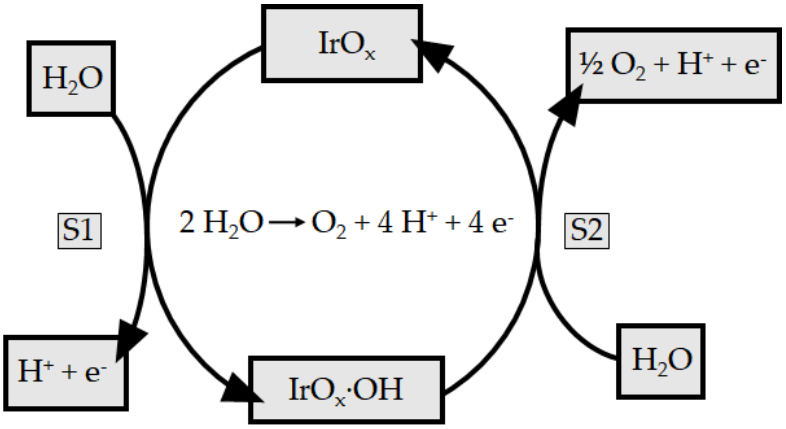

Figure 11. Typical water splitting path occurring when iridium oxide is used as catalyst.

In order to explain the exceptional capacity of iridium oxide loaded tungsten trioxide nanowires for detecting NO_2, the following mechanism is introduced. At high moisture levels, the interaction with water molecules resulting in the formation of surface hydroxyls is a competitive reaction with the adsorption of

NO_2 [22][23][24]. Surface hydroxyls would react with the highly available water molecules rather than with the traces of NO_2 and, this explains the significant decrease in response towards nitrogen dioxide observed under the presence of moisture. In contrast, when working under dry air conditions, the typical values of relative humidity found inside the test chamber range between 2% to 5%, therefore, a small water content is always present in the atmosphere surrounding the sensors. Under these conditions, few hydroxyl groups are found on the surface of iridium oxide nanoparticles and, NO_2 molecules can easily interact directly with the surface of iridium oxide, which results in a high response signal.

We will now further discuss the sensing mechanism for nitrogen dioxide under low moisture conditions. This is schematized in Figure 11. Following the water splitting reaction, when iridium oxide is present (**S1**) water molecules and radical hydroxyl groups become adsorbed (**S2**). This leads to the formation of –OOH groups, which have been reported to be found only during the oxygen evolution reaction. The formation of –OOH groups involves surface hydroxyls reacting with lattice oxygen species, changing the oxidation state of iridium to Ir(V) (**S3**) [25] [26]. When humidity is in the 2-5% range, NO_2 molecules can easily get adsorbed at the surface of iridium oxide. Adsorbed nitrogen dioxide (an electrophile) can subsequently react with atomic oxygen (a nucleophile), which is made available via the OER taking place at neighboring sites (**S4**). The higher the amount of iridium oxide nanoparticles is, the higher the production of free atomic oxygen is, and more NO_2 molecules react with these oxygen species resulting in the formation of NO_3^-. This increases the total electronic net charge transferred from the host material (i.e., WO_3), which translates into a high resistance change (as shown in Figure 1). When the atomic oxygen is released and captured by NO_2 molecules, iridium suffers a reduction from Ir(V) to Ir(III), leading to the formation of $HIr(III)O_2$ (**S5**) [27]. When the oxidation of Ir(III) to Ir(IV) occurs (**S6**), the surface of the catalyst is regenerated and a proton is

released, leading to the formation of hydrogen. This last step in which hydrogen is produced, could be the reason why the sensor responses towards hydrogen measured for this materials are so weak (see supporting information). The presence of physisorbed NO_2 and chemisorbed NO_3^- species has been confirmed by performing XPS analysis of a sensor exposed to NO_2 (these results can be found in the supporting information). Furthermore, the presence of IrO_2-OH moieties on the surface of the materials exposed to humidity has been confirmed by TOF-SIMS (these results are reported in the supporting information of this paper). These results taken together support the sensing mechanisms depicted in Figure 12.

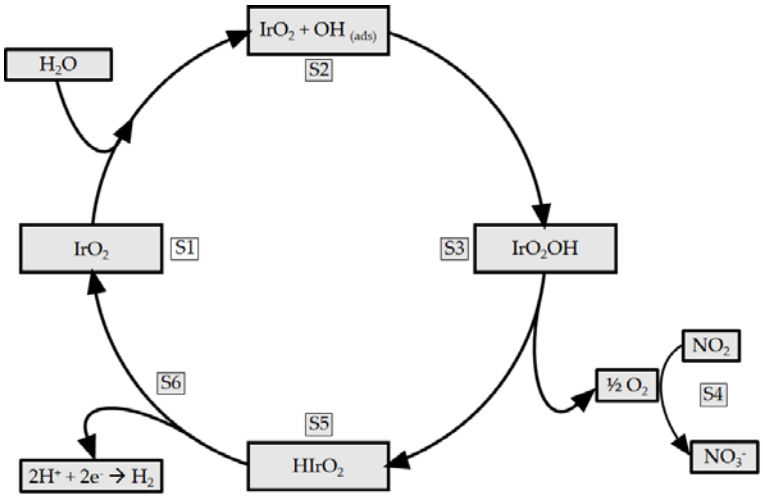

Figure 12. Schematic pathway mechanism towards the detection of NO_2 at very low relative humidity conditions.

A second plausible mechanism for the response enhancement upon IrO_2 loading, complementary to the above mentioned one, is the increase in the number of surface defects and the increased amount of oxygen species chemisorbed at the surface [23]. This is supported by baseline resistance measurements in pure and IrO_2 loaded tungsten oxide sensors (see the Supporting Information). The increase in the response obtained for both IrO_2/LC and IrO_2/HC can be attributed to the rough morphology of the nanowires, when these are loaded with IrO_2, which enhances the number of surface sites in which NO_2 molecules can be chemisorbed [24]. At the same time, a highly increased roughness makes more

difficult for chemisorbed species to leave the material surface and, thus, impeding new molecules to react. When considering sensors using IrO_2/LC, these experience an enhancement in their response towards NO_2 and no response saturation effects are seen. In contrast, sensors employing IrO_2/HC show a dramatically increased response towards NO_2, yet clear response saturation effects are observable within the concentration range tested.

4. Conclusions

Aerosol assisted chemical vapor deposition has been employed to grow tungsten trioxide nanowires loaded with iridium oxide from the precursors tungsten hexacarbonyl and pure iridium oxide powder. To ensure an efficient as well as a homogenous loading, a two-step procedure is followed. Furthermore, different levels of iridium oxide loadings have been achieved, displaying clear differences in gas sensing properties.

XRD has confirmed the synthesis of high-quality crystalline WO_3 NWs. HR-TEM and SEM analysis have shown the occurrence of morphology changes that correlate well with the increase in iridium oxide loading. These results are supported by a photoluminescence study, which reveals an increase in the number of surface defects, when comparing pure WO_3 NWs and IrO_2 loaded WO_3 NWs. XPS and ToF-SIMS analysis have been carried out to confirm the presence of iridium on the sensing layers.

The responses and sensitivity towards different gases, both reducing and oxidizing, of the different materials grown were studied. The loading of iridium oxide nanoparticles to the nanowire matrix dramatically increases the responsiveness towards nitrogen dioxide, as the loading of iridium oxide increases. In contrast, no effect or a slight response enhancement was observed for the other gaseous species tested. When IrO_2/HC samples (operated at 200 ºC) were exposed to 1 ppm of NO_2, their response was 95 times higher than the one measured for pristine nanowires. The mechanism behind this response

enhancement can be attributed to the catalytic properties of iridium oxide towards the water splitting reaction. In water splitting, the generation of atomic oxygen is dramatically increased, enabling its reaction with adsorbed nitrogen dioxide, thus enhancing sensor response. However, the mechanism that boost NO_2 response in IrO_2/HC samples is hindered at higher relative humidity levels. In contrast, IrO_2/LC samples operated at 150 ºC, show fair responsiveness to NO_2 at ppb levels. Furthermore, their responsiveness is little affected by humidity in the 2%-35% R.H. range tested. As a result, IrO_2/LC nanomaterials operated at 150 ºC show potential for being employed in resistive sensors to monitor the presence of NO_2 in the ambient (indoor/ outdoor), under real atmospheric conditions.

Conflicts of interest

There are no conflicts of interest to declare.

Acknowledgements

This work was funded in part by MINECO and FEDER via grants no. TEC2015-71663-R and RTI2018-101580-B-I00, by AGAUR under grant. 2017SGR 418 and by FNRS via PLAFON and FITTED projects. E.N. gratefully acknowledges a doctoral fellowship from MINECO grant no. BES-2016-076582. E.L. is supported by the Catalan institution for Research and Advanced Studies via the 2018 Edition of the ICREA Academia Award. C.B. is a research Associate of the FNRS (Belgium). F.G. is grateful to project MAT2017-87500-P.

References

[1] J. Watson, K. Ihokura, and G. S. V Coles, (1993). "The Tin Dioxide Gas Sensor," *Meas. Sci. Technol.*, vol. 4, no. 7, pp. 711–719.

[2] S. Vallejos, F. Di Maggio, T. Shujah, and C. Blackman, (2016) ."Chemical Vapour Deposition of Gas Sensitive Metal Oxides," *Chemosensors*, vol. 4, no. 1, p. 4.

[3] L. Zhou, Q. Ren, X. Zhou, J. Tang, Z. Chen, and C. Yu, (2018). "Comprehensive understanding on the formation of highly ordered mesoporous tungsten oxides by

X-ray diffraction and Raman spectroscopy," *Microporous Mesoporous Mater.*, vol. 109, no. 1–3, pp. 248–257.

[4] Y. S. Shim, L. Zhangd, D. H. Kimb, Y. H. Kimb, Y. R. Choib, S. H. Nahme, C.-Y. Kang, W. Leea, H. W. Jang, (2014)."Highly sensitive and selective H_2 and NO_2 gas sensors based on surface-decorated WO_3 nanoigloos," *Sensors Actuators, B Chem.*, vol. 198, no. 2, pp. 294–301.

[5] X. Gaoa, X. Sua, C. Yanga, F. Xiaoa, J. Wanga, X. Caob, S. Wangb, L. Zhang, (2013). "Hydrothermal synthesis of WO_3 nanoplates as highly sensitive cyclohexene sensor and high-efficiency MB photocatalyst," *Sensors Actuators, B Chem.*, vol. 181, pp. 537–543.

[6] X. C. Song, Y. F. Zheng, E. Yang, and Y. Wang, (2007). "Large-scale hydrothermal synthesis of WO_3 nanowires in the presence of K_2SO_4," *Mater. Lett.*, vol. 61, no. 18, pp. 3904–3908.

[7] H. Zheng, J. Z. Ou, M. S. Strano, R. B. Kaner, A. Mitchell, and K. Kalantar-Zadeh, (2011). "Nanostructured tungsten oxide - Properties, synthesis, and applications," *Adv. Funct. Mater.*, vol. 21, no. 12, pp. 2175–2196.

[8] H. Drug, O. Medoxomil, and A. Irshad, (2006). "Growth and characterization of well aligned densely packed IrO_2 nanocrystals on sapphire via reactive sputtering Growth and characterization of well aligned densely packed IrO_2 nanocrystals on sapphire via reactive," *J. Phys.: Condens. Matter.*,vol. 18, pp.1121–1136.

[9] Y.-T. Hsieh, L.-W. Chang, C.-C. Chang, and H. C. Shih, (2011). "Synthesis of WO_3 Nanorods by Thermal CVD at Various Gas Flow Rates and Substrate Temperatures," *Electrochem. Solid-State Lett.*, vol. 14, no. 7, p. K40-K42.

[10] F. E. Annanouch, Z. Haddi, M. Ling, F. Di Maggio, S. Vallejos, T. Vilic, Y. Zhu, T. Shujah, P. Umek, C. Bittencourt, C. Blackman and E. Llobet (2016). "Aerosol-Assisted CVD-Grown PdO Nanoparticle-Decorated Tungsten Oxide Nanoneedles Extremely Sensitive and Selective to Hydrogen." *ACS Applied Materials & Interfaces*, vol. 8, no. 16, pp. 10413–10421.

[11] S. Vallejos , P. Umek , T. Stoycheva , F. E. Annanouch , E. Llobet , X. Correig, P. De Marco, C. Bittencourt and C. Blackman (2013). "Single-Step Deposition of Au- and Pt-Nanoparticle-Functionalized Tungsten Oxide

Nanoneedles Synthesized Via Aerosol-Assisted CVD, and Used for Fabrication of Selective Gas Microsensor Arrays." *Advanced Functional Materials*, vol. 23, no. 10, pp. 1313–1322.

[12] F. E. Annanouch, Z. Haddi, S. Vallejos, P. Umek, P. Guttmann, C. Bittencourt and E. Llobet (2015). "Aerosol-assisted CVD-grown WO_3 nanoneedles decorated with copper oxide nanoparticles for the selective and humidity-resilient detection of H_2S," *ACS Appl. Mater. Interfaces*, vol. 7, no. 12, pp. 6842–6851.

[13] E. Navarrete, C. Bittencourt, P. Umek, and E. Llobet, (2018). "AACVD and gas sensing properties of nickel oxide nanoparticle decorated tungsten oxide nanowires," *J. Mater. Chem. C*, vol. 6, no. 19, pp. 5181–5192.

[14] A. Karthigeyan, R. P. Gupta, K. Scharnagl, M. Burgmair, S. K. Sharma, and I. Eisele, (2002) "A room temperature HSGFET ammonia sensor based on iridium oxide thin film," *Sensors Actuators, B Chem.*, vol. 85, no. 1–2, pp. 145–153.

[15] N. Yamazoe, G. Sakai, and K. Shimanoe, (2003). "Oxide semiconductor gas sensors," *Catal. Surv. from Asia*, vol. 7, no. 1, pp. 63–75.

[16] F. Güell, P. R. Martínez-Alanis, S. Khachadorian, J. Rubio-Garcia, A. Franke, A. Hoffmann, and G. Santana, (2016) "Raman and photoluminescence properties of ZnO nanowires grown by a catalyst-free vapor-transport process using ZnO nanoparticle seeds," *Phys. Status Solidi B*, vol. 253, no. 5, pp. 883–888.

[17] A. H. Romero, F. Widulle, R. Lauck, and M. Cardona, (2003) "Dispersive Phonon Linewidths : The E_2 Phonons of ZnO," *Phys. Review Letters,* vol. 90, no. 5, pp. 16–19.

[18] F. Güell and P. R. Martínez-Alanis, (2019) "Tailoring the Green, Yellow and Red defect emission bands in ZnO nanowires via the growth parameters," *J. Lumin.*, vol. 210, pp. 128–134.

[19] S. Cho, J. Jang, K. Lee and J. S. Lee, (2014). "Research Update : Strategies for efficient photoelectrochemical water splitting using metal oxide photoanodes Research Update : Strategies for efficient photoelectrochemical water splitting using metal oxide photoanodes," *APL Materials*, vol. 2, pp. 010703.

[20] S. Trasatti (1984). "Electrocatalysis in the anodic evolution of oxygen and

chlorine," *Electrochim. Acta*, vol. 29, no. 11, pp. 1503–1512.

[21] H. G. Sanchezcasalongue, M. L. Ng, S. Kaya, D. Friebel, H. Ogasawara, and A. Nilsson, (2014). "InSitu observation of surface species on iridium oxide nanoparticles during the oxygen evolution reaction," *Angew. Chemie - Int. Ed.*, vol. 53, no. 28, pp. 7169–7172.

[22] S. Roso, C. Bittencourt, P. Umek, O. González, Frank Güell, A. Urakawa and E. Llobet (2016). "Synthesis of single crystalline In $_2$ O $_3$ octahedra for the selective detection of NO_2 and H_2 at trace levels," *J. Mater. Chem. C*, vol. 4, no. 40, pp. 9418–9427.

[23] N. Barsan and U. Weimar, (2002) "Conduction Model of Metal Oxide Gas Sensors," *J. of Electroceramics*, vol. 7, pp. 143–167.

[24] A. Ponzoni, C. Baratto, N. Cattabiani, M. Falasconi, V. Galstya, E. Nunez-Carmona, F. Rigoni, V. Sberveglieri, G. Zambotti and Dario Zappa, (2017). "Metal Oxide Gas Sensors, a Survey of Selectivity Issues Addressed at the SENSOR Lab, Brescia (Italy)." *Sensors*, vol. 17, pp. 714.

[25] T. Nakagawa, C. A. Beasley, and R. W. Murray, (2009) "Efficient electro-oxidation of water near its Reversible potential by a mesoporous IrO_x nanoparticle film," *J. Phys. Chem. C*, vol. 113, no. 30, pp. 12958–12961.

[26] A. Minguzzi, O. Lugaresi, E. Achilli, C. Locatelli, A. Vertova, P. Ghignabc and Sandra Rondinini (2014). "Observing the oxidation state turnover in heterogeneous iridium-based water oxidation catalysts," *Chem. Sci.*, vol. 5, no. 9, pp. 3591–3597.

[27] O. Kasian, J. P. Grote, S. Geiger, S. Cherevko, and K. J. J. Mayrhofer, (2018) "The Common Intermediates of Oxygen Evolution and Dissolution Reactions during Water Electrolysis on Iridium," *Angew. Chemie - Int. Ed.*, vol. 57, no. 9, pp. 2488–2491.